Biosensors and Bioelectronics 199 (2022) 113862

Contents lists available at ScienceDirect

Biosensors and Bioelectronics

journal homepage: www.elsevier.com/locate/bios

An equivalent circuit model for localized electroporation on porous substrates

Justin R. Brooks [a], Ikhlaas Mungloo [a], Siamak Mirfendereski [a], Jacob P. Quint [a], Dominic Paul [a], Arian Jaberi [a], Jae Sung Park [a], Ruiguo Yang [b,*]

[a] Department of Mechanical and Materials Engineering, University of Nebraska-Lincoln, Lincoln, NE, 68588, USA
[b] Nebraska Center for Integrated Biomolecular Communication, University of Nebraska-Lincoln, Lincoln, NE, 68588, USA

ARTICLE INFO

Keywords:
Electroporation
Porous substrate
Localized cell electroporation
Circuit model

ABSTRACT

In vitro intracellular delivery is a fundamental challenge with no widely adopted methods capable of both delivering to millions of cells and controlling that delivery to a high degree of accuracy. One promising method is porous substrate electroporation (PSEP), where cells are cultured on porous substrates and electric fields are used to permeabilize discrete portions of the cell membrane for delivery. A major obstacle to the widespread use of PSEP is a poor understanding of the various impedances that constitute the system, including the impedances of the porous substrate and the cell monolayer, and how these impedances are influenced by experimental parameters. In response, we used impedance measurements to develop an equivalent circuit model that closely mimics the behavior of each of the main components of the PSEP system. This circuit model reveals for the first time the distribution of voltage across the electrode-electrolyte interface impedances, the channels of the porous substrate, the cell monolayer, and the transmembrane potential during PSEP. We applied sample waveforms through our model to understand how waveforms can be improved for future studies. Our model was validated from intracellular delivery of protein using PSEP.

1. Introduction

Reversible electroporation is one of the most used methods for intracellular delivery alongside viral and chemical vectors (Stewart et al., 2016). Electroporation involves subjecting cells to an electric field to induce reversible permeabilization of the cell membrane for delivery or extraction of drugs, proteins, and nucleic acids (Cervia and Yuan, 2018; Shi et al., 2018a), or to induce irreversible permeabilization for tumor ablation (Aycock and Davalos, 2019). The most common form of electroporation is bulk electroporation, where millions of cells are suspended and electroporated within a cuvette. Porous substrate electroporation (PSEP) is an alternative high throughput method that allows delivery to cells in adherent culture conditions, thus reducing stress and allowing electroporation on sensitive cells, such as primary cells and stem cells (Chang et al., 2016c; Shi et al., 2018b). During PSEP, cells are cultured on porous membranes (Mukherjee et al., 2020) or silicon chips (Dong et al., 2020) so that only regions of the cell over the micro- or nanochannels in the substrate are exposed to the electric field and undergo permeabilization. The total area of the cell exposed to the electric field can be far below 1% (Cao et al., 2019b), reducing stress on the cell. Many studies have utilized PSEP for delivery, but the underlying delivery mechanism remains relatively unexplored. Some differences between PSEP and bulk electroporation that require additional investigation are the role of channel geometry and materials on transport through the substrate, the reduced role of endocytosis on membrane transport, and the role of cellular adhesion on pore formation and intracellular transport to the nucleus. Researchers using PSEP and similar methods such as nanostructure electroporation have hypothesized that strong electric fields occur within the channels, making electrophoresis the primary mechanism of delivery (Chang et al., 2015a; Chen et al., 2016; Fei et al., 2007; Khine et al., 2007). However, the magnitude of the electric field within the channels has not been experimentally determined, making it difficult to assess the role of electrophoresis in the delivery process. Indeed, most of the theoretical understanding of the PSEP process is based on simulations of a single cell over a single channel (Chang et al., 2015b; Fei et al., 2010) and these simulations do not include the influences of the surrounding cells and channels. Furthermore, there is not a consensus regarding the

* Corresponding author.
E-mail address: ryang6@unl.edu (R. Yang).

https://doi.org/10.1016/j.bios.2021.113862
Received 10 August 2021; Received in revised form 29 November 2021; Accepted 2 December 2021
Available online 10 December 2021

importance of cell confluency on delivery with these and related systems; some researchers suggest confluency must be above a certain value for electroporation to occur (Mukherjee et al., 2018) and others claim it is insignificant (Cao et al., 2018). Additionally, the roles of parameters such as electrolyte composition and conductivity, ambient temperature, electrode distance, channel size and density, cell type, and waveform selection require further study, making comparisons between studies difficult. Impedance measurements of PSEP systems are not often published (Fei et al., 2013), and electrode-electrolyte interface (EEI) impedances in particular have not been accounted for in PSEP simulations. EEI impedances are caused by electrochemical reactions and the electrical double layer formed when ions adsorbed to the surface of the electrode interact with diffuse ions present in the electrolyte (Epelboin et al., 1973). These impedances can be very large and are inversely dependent on voltage (Mayer et al., 1992). Some authors have discussed the impedances that occur at the electrode-electrolyte interface (Huang and Rubinsky, 2001; Mukherjee et al., 2018), but simulations thus far have utilized a far-field voltage in the electrolyte as a boundary condition rather than the known voltage applied at the electrodes. Without accounting for the EEI impedances, it is difficult to predict the far-field voltage from an applied voltage at the electrodes.

The electroporation process is dependent on the voltage and the corresponding electric field present at different points in the system. Therefore, to understand the underlying delivery mechanisms and thus improve PSEP so that it can fulfill the many applications of *in vitro* intracellular delivery, the relationship between the applied voltage and the voltage experienced at different points in the system needs to be investigated. The voltage at different points in the system, which are often frequency and waveform-dependent, are difficult to understand without a circuit model which accounts for all relevant system impedances based on experimental data. Circuit models have been used to understand similar electrochemical systems (Kang et al., 2014), including systems containing porous substrates such as batteries (Zhang et al., 2017) and supercapacitors (Zhang et al., 2018). Thus, a circuit model that reflects the macroscale environment is needed to improve simulations of individual substrate channels and cells. For example, although individual channels have very large impedance values, they must be analyzed in the broader context of the numerous parallel channels to determine if they contain a large electric field. Higher quantities of parallel channels reduce the impedance of the substrate, and therefore reduce the electric field generated in the channels.

To help clarify the underlying phenomena and improve upon existing PSEP simulations, we have constructed a macroscale circuit model of PSEP systems using experimentally measured impedance values. Our model quantifies the impedance contributions of the major components of the PSEP system, including the combined EEI and bulk electrolyte impedance, the substrate impedance, and the cell monolayer impedance. We used this model to simulate the voltage drop across each circuit element with different waveform voltage amplitudes, pulse widths, and frequencies, and to estimate the resulting transmembrane potential (TMP). Our model was validated using electroporation with different voltages, seeding densities, and electrolytes.

2. Materials and methods

2.1. Device fabrication

PDMS molds were printed with a Stratasys Objet 500 Connex3 3D printer using VeroClear. After removal of support material, molds were baked at 80°C for 8 h. Without baking, PDMS did not crosslink at the PDMS-VeroClear interface. After degassing, substrates (polycarbonate membranes, it4ip, Belgium) were placed in molds and the two sides of the molds were screwed together. PDMS was added to the molds using a syringe through fill holes in the upper surface. The molds were baked at 80°C for 1 h and the devices were ready for use. After the PDMS was cured around the substrate in the mold, it was retained within the mold for the duration of the experiment. Following an experiment, the molds were separated and the PDMS sheet with embedded substrates was removed and discarded.

2.2. Cell culture

Devices were sterilized with 70% ethanol and UV light for 1 h. After sterilization, devices were soaked in distilled water to remove remaining ethanol. A 5 μg/mL fibronectin solution in phosphate-buffered saline (PBS) was added to the wells and incubated at 37°C overnight to allow increased cell-substrate adhesion. The fibronectin solution was removed, and the wells were washed with distilled water twice and cell culture media once. HEK293 cells (ATCC) were seeded in the wells 12 h prior to experiments to allow sufficient adhesion. HEK293 cells were chosen because they are commonly used for electroporation. Cell culture media consisted of Dulbecco's modified Eagle's medium (DMEM) (Gibco) with 10% v/v fetal bovine serum (FBS) (Gibco) and 1% v/v penicillin-streptomycin (Gibco).

2.3. Impedance measurements without cells

A Keysight U2761A function generator was used to generate alternating current (AC) sine waves with amplitudes of 40 mV to 5V and frequencies of 10Hz–3000Hz. The measured root-mean-square (RMS) voltage across a known load was used with the known AC input at frequencies ranging from 10 to 3000Hz to approximate the impedance of the function generator. The RMS voltage across the load was measured using a National Instruments USB-4065 digital multimeter. For voltages higher than 5V, a Taidacent OPA541 amplifier was used.

2.4. Seeding density impedance measurements

Cells were seeded the night before at various seeding densities. Propidium iodide (Invitrogen) was added at a concentration of 5 μg/mL (7.5 μM) prior to applying the waveform to ensure the waveform did not cause permeabilization or death. Impedance measurements were obtained using a 2.5V amplitude sinusoidal waveform while the cells were incubated. After measuring, calcein AM (Invitrogen) was added to the cell culture chambers to assess viability at a final concentration of 5 μg/mL (8 μM) and cells were incubated for 5 min. Only living cells were assessed because dead cells were assumed to have reduced adhesion and thus a reduced impact on system impedance. Composite images consisting of 9 images per well were obtained using a Zeiss Axio Observer 5 fluorescent microscope.

2.5. Impedance calculation

The magnitude of the load impedance was approximated from the RMS voltage using the following equation:

$$|Z| = \left(\frac{V_{rms,load}}{V_{rms,source} - V_{rms,load}}\right)\left(\frac{1}{C_O \cdot 2\pi f} + R_O\right) \quad (1)$$

where $|Z|$ is the magnitude of the load impedance; $V_{rms,load}$ is the RMS voltage across the load impedance; $V_{rms,source}$ is the RMS voltage applied by the function generator; C_O is the equivalent capacitance of the function generator, measured to be 2 mF; and R_O is the equivalent resistance of the function generator, measured to be 50Ω.

2.6. Circuit model simulation of different waveforms

The MATLAB code used for these simulations is available for download at https://github.com/YangLabUNL/PSEP_circuit_model. The combined EEI and bulk electrolyte impedance was calculated at multiple voltages using the experimentally determined voltage relationship. For unilevel square waves, impedances were calculated at a

high voltage and 0 V. High voltages that were investigated include 4, 5, 6, 25, and 125 V. For bilevel square waves, the impedances were calculated at 25 V, 5 V, and 0 V. For exponential waves impedances were calculated at 100 linearly spaced voltages from 0 to 25 V. A 100-term Fourier series was calculated for the waveform applied to the circuit. The Laplace transform was calculated for each term in the Fourier series. Fourier terms were analyzed separately before summing to reduce computational complexity. The Laplace transforms were substituted into the following equations which describe the magnitude of the voltage across the combined EEI and bulk electrolyte impedance (V_E) and substrate impedance (V_S), respectfully, in the frequency domain:

$$V_E(s) = \frac{V_{source}(s)Z_E}{Z_E + Z_S + Z_C} \tag{2}$$

$$V_E(s) = \frac{V_{source}(s)Z_S}{Z_E + Z_S + Z_C} \tag{3}$$

The inverse Laplace transforms of Eqs. (2) and (3) were calculated at each of the combined EEI and bulk electrolyte impedance voltages mentioned earlier for each term in the Fourier series. Each series of inverse Laplace transforms were summed to produce an equation for the voltages across the EEI and substrate impedances in the time domain. The voltage across the cell monolayer was calculated as the difference between the applied voltage and the voltage across the EEI and substrate impedances. The TMP was calculated as 80% of the voltage drop across the cell monolayer.

2.7. Electroporation

Cells were removed from the incubator and the cargo chamber was filled with 2.5 mg/mL bovine serum albumin (BSA) conjugated with Alexa Fluor 555 or Alexa Fluor 647 (Invitrogen) in PBS (Gibco) or hypo-osmolar buffer (HOB) (Cole-Parmer). For some experiments, the DMEM in the cell culture chamber was replaced with HOB to assess the influence of electrolytes on electroporation. The device was placed in the fixture and gold-plated electrodes were inserted into the chambers. The fixture was transferred to the incubator and the electrodes were plugged into a Bio-Rad Gene Pulser II Electroporation System with RF Module. 400 unilevel square electric pulses were generated with 3 ms pulse duration, 500 ms pulse interval, and various voltages. Electrodes were used only once due to corrosion and polarization from the electric pulses.

2.8. Imaging

After electroporation, both chambers were washed twice using DMEM, then the culture chamber was filled with DMEM containing 5 μg/mL of calcein AM and 20 μg/mL of Hoechst 33342 (Invitrogen). Cells were washed after all six wells had been electroporated, meaning the first wells were washed approximately 20 min after pulses were applied and the last wells were washed immediately. We did not observe a trend in viability or delivery based on well number. Cells were incubated at 37°C with 5% CO_2 for 5 min before the chambers were inverted and imaged using a Zeiss Axio Observer 5 fluorescent microscope. Hoechst 33342 was used to quantify the total cells and calcein was used to quantify viability. Total delivery was determined from the number of cells containing BSA as a fraction of total cells. Delivery efficiency was determined from the number of cells with simultaneous BSA and calcein internalization as a fraction of total cells.

3. Results and discussion

3.1. A high throughput electroporation and electrical measurement platform

Many PSEP parameters remain poorly understood because PSEP is time-consuming and labor-intensive. PSEP often requires new devices for each experiment, to ensure the narrow channels are free of previous cargos and biological materials. Therefore, prior to conducting experiments we developed a method of creating PSEP chambers using PDMS cured in 3D printed molds (Fig. 1A–B, Figs. S1 and SI). This process facilitates parallel and high throughput impedance measurements and electroporation. In addition, PDMS molds have advantages including more consistent shape and size, and increased throughput and robustness from eliminating steps involving sealing two separate cell culture wells around the substrate. Each mold contains multiple wells allowing multiple samples to be prepared simultaneously (Fig. 1C). Furthermore, we modified PSEP by rotating the substrate vertically (Fig. 1D). The liquid in the chambers is held in place by capillary action. Positioning the substrate vertically removes the step of sealing the lower well to the lower electrode, increasing throughput.

Devices were evaluated for substrate properties and biocompatibility. Scanning electron microscope (SEM) images of substrates show channels of the approximate size and density specified by the manufacturer (Fig. 1E). Channels are randomly spaced throughout the substrate and some deviate significantly from perpendicular to the surface. HEK293 cells were cultured in the wells with high viability, and we observed no changes in cell morphology or proliferation rate (Fig. 1F). Each well can contain approximately 40,000 cells per well for a total of 240,000 cells per mold. The cell culture chamber can hold 45 μL of cell culture media, which is sufficient for overnight culture at high confluency. Each culture chamber is 2 mm deep to allow cells to be imaged on the substrate using an inverted microscope when the mold is inverted.

3.2. An equivalent circuit model based on measured impedance of the electroporation system

We developed an equivalent circuit model using impedance measurements of increasingly complex configurations of PSEP to determine the contributions of different elements (Fig. 2), including the substrate, bulk electrolyte, electrodes, and cell monolayer. Each impedance value can be found in Table 1. The function generator impedance was measured using a voltage divider consisting of the function generator and known resistors and capacitors. The frequency range was chosen to encompass frequencies commonly used for PSEP (Brooks et al., 2020), although the minimum frequency was limited to 10Hz because lower frequencies yielded inaccurate RMS voltage values. The function generator resistance in our model agrees with the 50Ω impedance specified by the manufacturer, and the resistance and capacitance in our model produced load voltages matching the voltages measured across different resistors and capacitors (Fig. 2B).

Using the function generator impedance, a voltage divider was used to measure the impedance of wells filled with PBS without substrates (Fig. 2C). This impedance consists of the voltage-dependent EEI impedance and the bulk electrolyte impedance. Above approximately 20 mV EEI impedances become highly nonlinear (Fasmin and Srinivasan, 2017; Lasia, 2014), resulting in impedances measured at lower voltages being several orders of magnitude higher than impedances measured at higher voltages. Each voltage also exhibited decreasing impedance with increasing frequencies, indicating capacitive effects. The combined EEI and bulk electrolytic impedance was modeled as a variable resistor in parallel with a series variable capacitor, variable resistor, and constant resistor. A resistor and capacitor in parallel were used to produce the voltage exponential decay that occurs at low frequencies. Additional resistors were used to shift the function upwards to reproduce the high frequency behavior. Variable resistors and capacitors were used to represent the voltage dependence of the impedance. EEI impedances are dependent on electrodes and electrolytes, so conditions used by other researchers may have higher or lower EEI impedances.

To measure the substrate impedance, measurements were repeated for devices with substrates of different channel size, channel density,

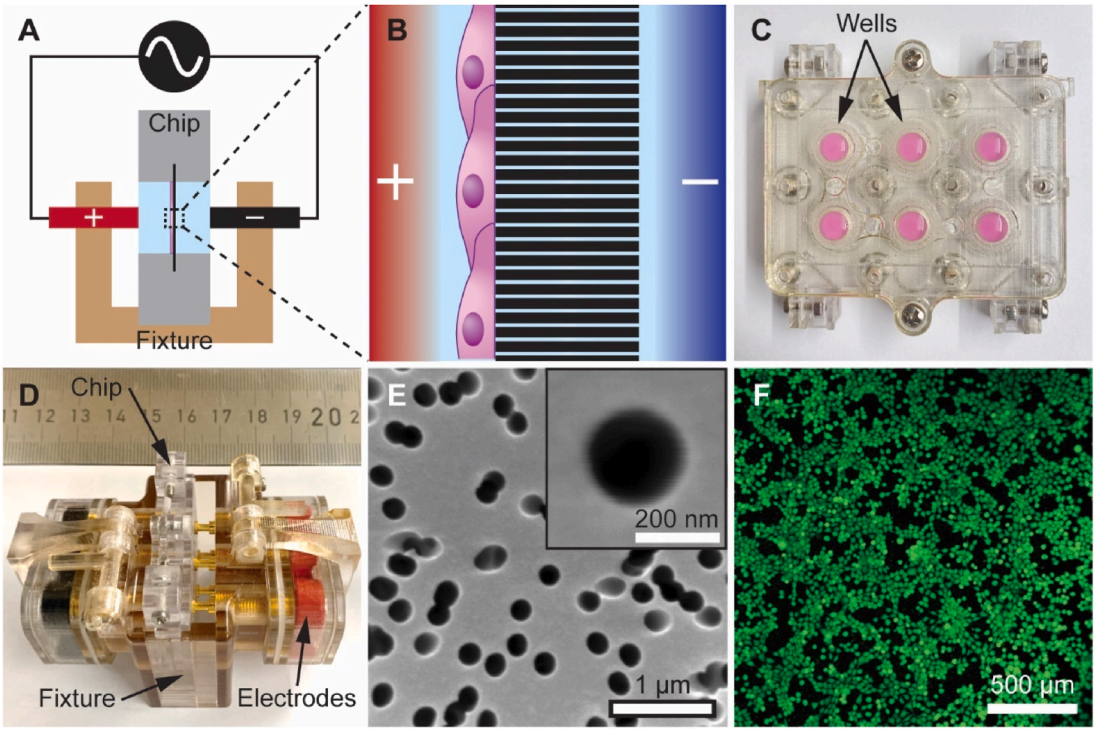

Fig. 1. System overview. A. Depiction of the mold placed in the fixture for electroporation. The electrodes are in contact with the culture and cargo chambers and connected to a function generator. The electrode polarity shown is for delivery of negatively charged cargo. **B.** Enlarged depiction of the cells on the substrate. **C.** Image of the 3D printed mold with DMEM in each well. **D.** Image of the assembled mold and fixture with a metric ruler for scale. **E.** SEM image of a 200 nm substrate without cells with a higher magnification image of a single channel. **F.** Image showing viability of cells stained with calcein and PI after being cultured in the device.

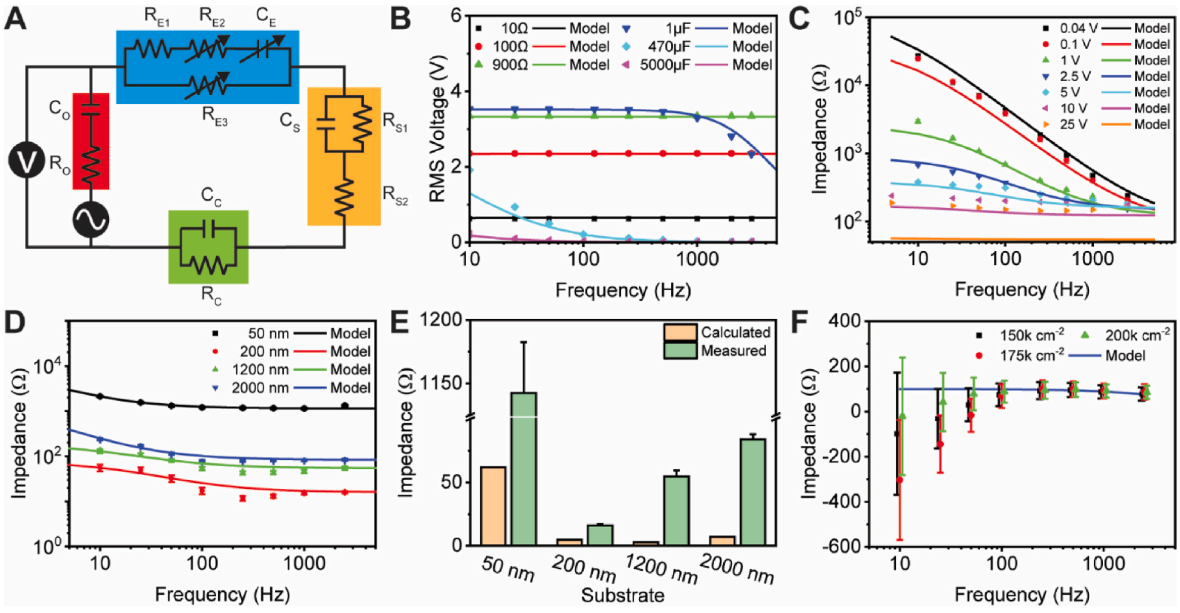

Fig. 2. An equivalent circuit model for PSEP systems. A. Circuit model with a voltmeter attached in a voltage divider configuration for impedance measurements. Red impedances represent the function generator impedances, blue impedances represent the combined EEI and bulk electrolyte impedances, gold impedances represent the substrate impedances, and the green resistor represents the cell monolayer impedance. **B.** RMS voltage versus frequency for known loads (n = 5) and corresponding values predicted using the function generator impedances in our model. **C.** Impedance versus frequency at multiple voltages for the combined EEI and bulk electrolytic impedances (n = 12) and corresponding values predicted by our model. **D.** Impedance versus frequency of substrates (n = 12) and corresponding values predicted by our model. **E.** Comparison between substrate impedances calculated using resistivity equations and measured substrate impedance values (n = 12). **F.** Impedance versus frequency of confluent samples (150, 175, and 200 thousand cells·cm^{-2}) subtracting the impedance of unseeded samples (n = 6), and the corresponding 90Ω resistance used in the model. Values in 2F are slightly horizontally shifted for clarity. Error bars are present in 2B–2F and represent the standard error of the mean. (For interpretation of the references to colour in this figure legend, the reader is referred to the Web version of this article.)

Table 1
Circuit model impedances.

Section	Circuit Element	Value
Function Generator	C_O	2000 μF
	R_O	50.176Ω
EEI and Bulk Electrolytic (PBS)	C_E	$2.0365*V^{0.5594}$μF
	R_{E1}	89.844Ω
	R_{E2}	35.441*V·Ω
	R_{E3}	$2532.7*V^{-1.176}$Ω
50 nm Substrate	C_S	14.852 μF
	R_{S1}	11130Ω
	R_{S2}	1142.4Ω
200 nm Substrate	C_S	140.74 μF
	R_{S1}	61.580Ω
	R_{S2}	16.055Ω
1200 nm Substrate	C_S	95.155 μF
	R_{S1}	133.15Ω
	R_{S2}	54.655Ω
2000 nm Substrate	C_S	88.297 μF
	R_{S1}	1927.7Ω
	R_{S2}	83.890Ω
Cell Monolayer	C_C	0.2 μF
	R_C	100Ω

and thickness (Fig. 2D). Substrates with 50, 200, 1200, and 2000 nm channels were measured. Additional substrate properties can be found in Table S1. The EEI and bulk electrolytic impedance was subtracted from the total impedance to estimate the substrate contribution. The 50 nm substrates had the highest impedance of any substrates, but counterintuitively, the 200 nm substrates had the lowest impedance. The substrate impedances were approximated with a parallel resistor and capacitor, both in series with a resistor. Similar to the combined EEI and bulk electrolyte impedance, the parallel resistor and capacitor were used to reproduce the exponential decay and the additional resistor was used to reproduce the high frequency behavior. Each substrate has a separate set of values for these three elements. We did not observe a trend in these element values across substrates, possibly because parameters such as substrate thickness, pore diameter, and pore density were varied simultaneously. Substrate impedances at 2500Hz were compared to the theoretical resistance of each substrate calculated using the formula for resistivity $R = \frac{L}{\sigma A}$, where σ is the PBS conductivity, L is the substrate thickness, and A is the total cross-sectional area of all the substrate channels in the well (Fig. 2E). The PBS conductivity was measured 1.75S/m. The impedance at 2500Hz was used to minimize substrate capacitance. The measured substrate impedances are much higher than the calculated impedances, likely because resistivity equations do not apply in smaller channels. Resistivity equations do not account for surface charges on channel walls that influence a large percentage of ions within smaller channels (Kemery et al., 1998; Yang, 2018). The influence of surface charges can be counteracted by increasing the number of free ions using electrolytes with high ionic concentration (Cornelius et al., 2007; Yang, 2018), but these electrolytes are toxic to cells and do not reflect PSEP conditions. Angled channels may also contribute to the discrepancy between the measured and calculated values.

Cells were cultured on substrates to determine their impedance. The substrates were coated with fibronectin and cells were cultured overnight at seeding densities ranging from no cells to 200,000 cells/cm^2 (40,000 cells per well). The DMEM in the cell culture chamber was replaced with fresh DMEM and HOB was added to the cargo chamber prior to measuring. Impedance measurements were recorded in an incubator to minimize stress on the cells. Measurements were recorded at 2.5V and the same frequencies as the other measurements. Cells were stained with calcein and imaged to confirm viability and confluency after each measurement. Confluencies corresponding to each seeding density can be found in Table S2. There was no correlation between confluency and impedance at low frequencies (Figs. S2 and SI), but at high frequencies, the cell monolayer impedance was significant above 125,000 cells/cm^2. Above 150,000 cells/cm^2, higher seeding densities did not cause an increase in impedance. Together, the impedance measurements and fluorescent images show the cell monolayer impedance is not significant until nearly 100% confluency has been achieved, after which there is no further increase in impedance. We observed no correlation between seeding density and impedance when cells were given less than 12 h to adhere. Our hypothesis is reduced adhesion time results in greater current leaking at channel openings due to decreased adhesion strength and reduced spreading.

We subtracted the impedance measured without cells from the impedance measured with seeding densities of 150, 175, and 200 thousand cells/cm^2 to determine the cell monolayer impedance at approximately 100% confluency (Fig. 2F). At low frequencies, the difference in impedance is negative, perhaps because of the discrepancy between our EEI model and the EEI measurements as seen in Fig. 2C. Previous studies have shown cell monolayers behave as resistors and capacitors in parallel, with the impedance approximately constant below 1 kHz and decreasing to almost zero at frequencies above 10 kHz (Cacopardo et al., 2019; Linz et al., 2020). Cell monolayer resistances have been reported ranging from less than 10Ωcm^2 to over 1000Ωcm^2 (Cereijido et al., 1978; Erben et al., 1995). Similarly, we measured our cell monolayer resistance to be approximately 100Ω, or 20Ωcm^2. 2.5 kHz was chosen as the upper limit of our measurements because our model is intended to aid in understanding PSEP, which thus far has been limited to pulse frequencies of 200Hz and below (Brooks et al., 2020). As a result, the high frequency behavior of our model is uncertain, but we chose a cell monolayer capacitance of 0.2 μF, or 1 μF/cm^2 because this capacitance is consistent with previously reported values of 1–10 μF/cm^2 (Bertrand et al., 1998; Linz et al., 2020; Wegener et al., 1996) and is in good agreement with our data, as shown in Fig. 2F. Unlike some models of cell impedance (Susloparova et al., 2013), our model neglects the leakage current at the cell-substrate interface due to the difficulty in determining this current at the macro-scale. However, cells in our experiments were allowed to adhere at least 12 h to reduce the influence of these currents. To observe whether the cell monolayer impedance varied with voltage, we measured the monolayer impedance with amplitudes of 2.5V (Figs. 2F) and 8V (Figs. S3 and SI). Significant necrosis was observed at amplitudes of 5V or greater through simultaneous PI internalization and calcein exclusion. Similar to the measurements at 2.5V, at 8V unseeded wells and wells seeded with 200,000 cells/cm^2 were measured and the unseeded well impedance was subtracted from the seeded well impedance. Extensive necrosis was visible at the higher voltage, yet the monolayer impedance was approximately equal at both voltages. Although we expected the monolayer impedance to decrease at higher voltages, the lack of change in impedance may be due to the low percentage of total cell membrane surface area permeabilized during PSEP.

Measuring the cell monolayer impedance allows us to estimate the TMP that occurs with various waveforms. The cell monolayer impedance consists of three impedances: the basal cell membrane, cytoplasm, and apical cell membrane. The voltage across the basal cell membrane is the TMP. The cell membrane has a much higher impedance than the cytoplasm (Kang et al., 2013), and the surface area of the basal cell membrane over the channels is much smaller than the surface area of the apical cell membrane, making the basal cell membrane the largest of the three impedances. Assuming the resistivity and thicknesses of the basal and apical cell membranes are equal, and the 1200 nm substrate has a porosity (p) of 24.9%, while neglecting the impedance of the cytoplasm, we get Eq. (4):

$$V_{basal} = \frac{V_{monolayer}}{1+p} = 0.801 V_{monolayer} \tag{4}$$

Thus, the TMP estimated from Eq. (4) is 80% of the voltage across the cell monolayer. An expanded derivation of the TMP is located in the supporting information.

3.3. Effects of electrical waveforms on the voltage across different circuit components

The circuit model was used to calculate the voltage drop across the combined EEI and bulk electrolytic impedance, substrate, cell monolayer, and TMP when different waveforms were applied (Fig. 3). The MATLAB code used for these calculations can be downloaded at the location in the materials and methods section. 20Hz square waves with 10 ms pulse duration and 40 ms pulse interval at voltages of 5, 10, and 25V and impedances of PBS, a 1200 nm substrate, and a confluent cell monolayer were used to demonstrate the effect voltage has on the voltage drop across each of the three main impedances and the TMP (Fig. 3A–C). Although recent bulk electroporation studies have utilized nanosecond pulse duration (Gianulis et al., 2015) and MHz frequencies (Ruzgys et al., 2019), our analysis is limited to values used for PSEP in the literature (Brooks et al., 2020). Fig. 3A–C demonstrate the non-intuitive changes that occur when different waveforms are applied, namely the nonlinear voltage relationship and the differences in charging and discharging of different components during each pulse. Higher voltage resulted in a higher proportion of the voltage drop occurring across the substrate and cell monolayer. The effects of different configurations of resistors and capacitors on charging rates and magnitudes can also be seen within each pulse duration. The circuit impedances charge much slower than they discharge due to the voltage dependency of the EEI capacitance. To account for permeabilization of the cell membrane that occurs after a critical TMP of 0.2–1V is exceeded, the TMP is limited to 1V or less. Corresponding electric field values for the different system components can be found in Table S3. The effect of different waveform shapes was also observed by simulating bi-level square pulses and exponential decay pulses (Figs. S4 and SI).

The influences of voltage, pulse frequency, and pulse duration on the distribution of voltage among the three impedances and the TMP were each analyzed over multiple conditions (Fig. 3D–F). The influence of applied voltage on voltage division was determined by producing waveforms similar to those in Fig. 3A–C at 8 different voltages ranging from 0.1V to 25V. The average percent contribution from each impedance and the percentage constituting the TMP was recorded at each condition as shown in Fig. 3D. Like the waveforms in Fig. 3A–C, the combined EEI and bulk electrolyte impedance is dominant at low voltages and the substrate and cell monolayer impedances are dominant and similar in magnitude at higher voltages, with the midpoint occurring at approximately 15V. To observe the influence of frequency, the waveform shown in Fig. 3B was simulated at frequencies ranging from 0.5Hz to 50Hz (Fig. 3E). No influence due to frequency was observed because the system rapidly discharges after each pulse. The influence due to pulse width was observed by simulating the waveform shown in Fig. 3B with pulse widths ranging from 0.5 ms to 100 ms (Fig. 3F). With a pulse width of 0.5 ms, the largest voltage drop occurs across the combined EEI and bulk electrolyte impedance, followed by the cell monolayer impedance, and the substrate impedance. At longer pulse widths, the substrate contributes a larger portion of the system impedance due to continued charging of the substrate capacitance, while the other impedances decrease in magnitude.

These simulations show how much the applied voltage drops across the EEI impedance before reaching the channels and cell membrane. Moreover, the voltage dependency of this impedance complicates conclusions made by researchers about pore evolution and the optimal voltage for delivery of different sized cargos (Cao et al., 2019a; Mukherjee et al., 2018; Shiva Nathamgari et al., 2019), since the transmembrane potential does not increase linearly with increases in voltage between the electrodes. In addition to the voltage drop at the electrode-electrolyte interface, understanding the voltage drop through the channels is important for predicting the electrokinetics of cargo transported through them. Many studies have calculated that most of the voltage drop in the system occurs across the channels (Bertani et al., 2015; Cao et al., 2019b; Chang et al., 2016a, 2016b). In contrast, our model predicts lower electric fields across the substrate and basal cell membrane at low voltages than simulations which neglect the EEI impedance and its voltage dependent behavior. At voltages of 25V or greater, our model is in closer agreement with other simulations due to the large decrease in the influence of the EEI impedance. Without impedance measurements of the substrates used in other studies, it is

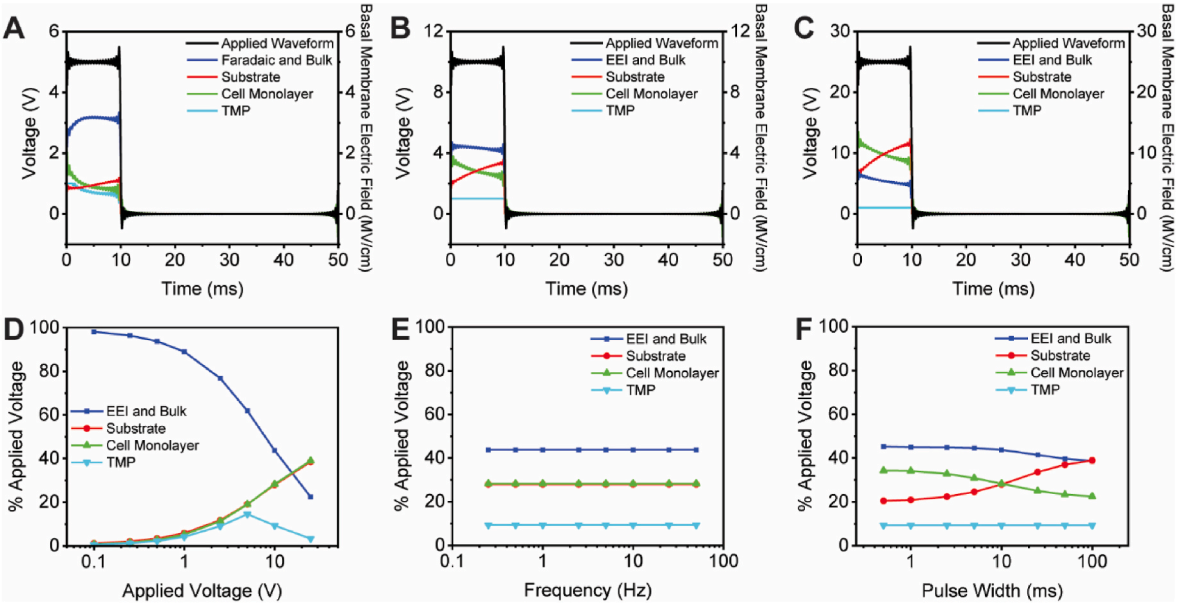

Fig. 3. Voltage distribution across PSEP components with applied waveforms. A-C. Waveforms applied to our model at 5, 10, and 25V showing the relative influences of the combined EEI and bulk electrolytic impedance, substrate impedance, cell monolayer impedance, and TMP changing with voltage and time. The model conditions are PBS, a 1200 nm substrate, and a confluent cell monolayer. Each wave has a pulse width of 10 ms and a pulse frequency of 20Hz. The TMP is defined as 80% of the cell monolayer voltage but is limited to 1V or less due to cell membrane permeabilization. **D.** Percentage of applied voltage across each element as a function of voltage for a 10 ms, 20Hz square wave. **E.** Percentage of applied voltage across each element as a function of pulse frequency for a 10V, 10 ms square wave. **F.** Percentage of applied voltage across each element as a function of pulse width for a 10V, 20Hz square wave.

unclear whether their substrates have much higher impedances or whether the voltage drop is occurring at other points in the system such as the EEI impedance.

3.4. Circuit model validation through electroporation

HEK293 cells were electroporated under various conditions with the dual purpose of validating our model and demonstrating that our model could be used to streamline parametric selection such as the voltage necessary for electroporation to occur. Fluorescently-tagged bovine serum albumin (BSA) was chosen as the cargo because it allows delivery to be observed immediately without transcription, translation, or nuclear delivery. The effects of voltage, electrolytes, and seeding density on viability, total delivery, and delivery efficiency were observed (Fig. 4). In this study, viability is defined as the percentage of cells alive after electroporation. Total delivery is defined as the percentage of cells containing BSA, regardless of whether the cells survived. Delivery efficiency is defined as the percentage of living cells containing BSA. Viable

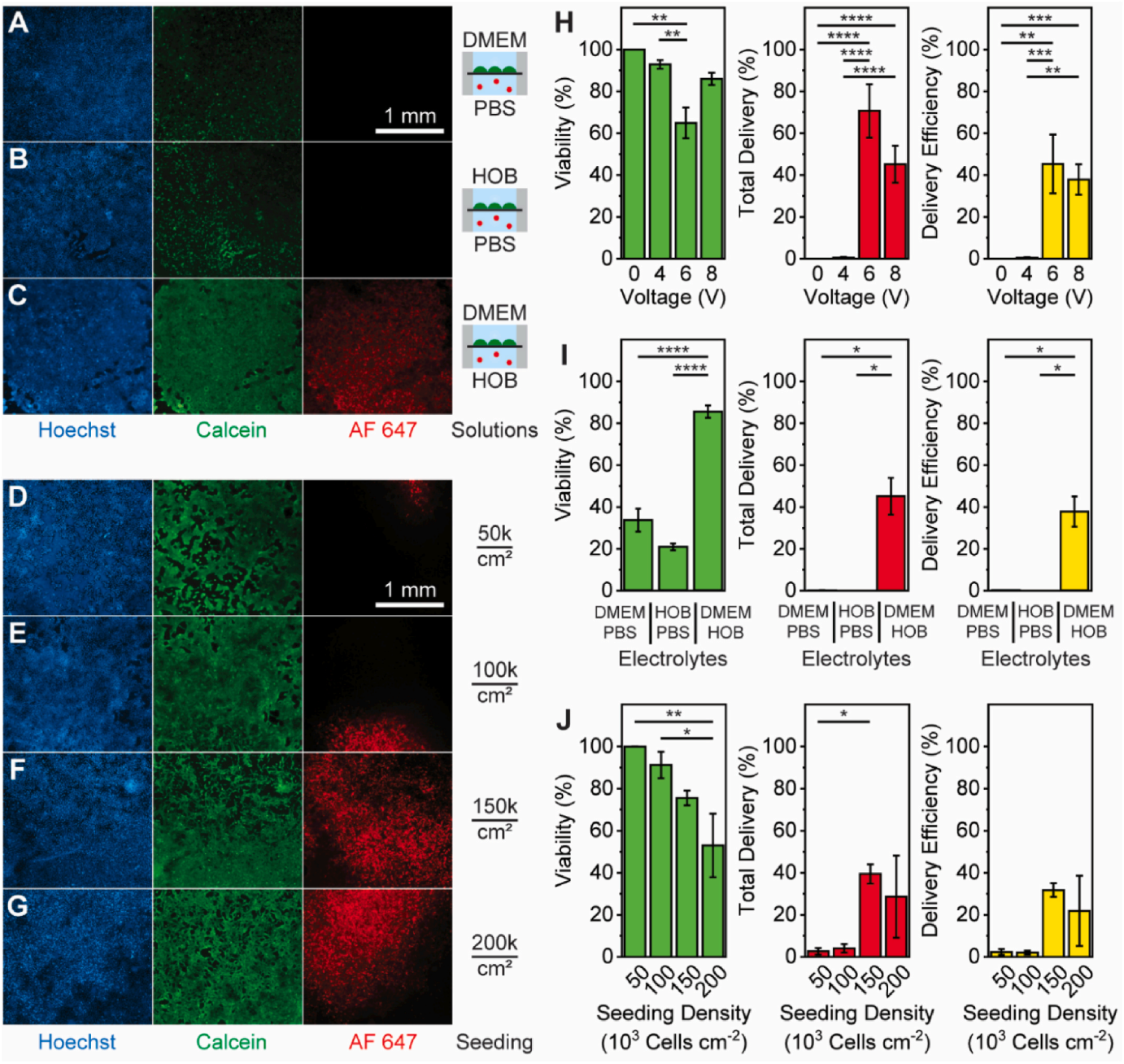

Fig. 4. Influence of voltage, electrolytes, and seeding density on electroporation. The electroporation parameters for each sample were 400 unilevel square pulses at 0.5 Hz with 3 ms pulse duration. **A-C.** Fluorescent microscope images of cells after electroporation when different electrolytes (DMEM, PBS, and HOB) are used in the cell culture and cargo chambers. **D-G.** Fluorescent microscope images of cells after electroporation when different seeding densities are electroporated. **H.** Percentage of cells viable, delivered to, and delivery efficiency at different voltages. **I.** Percentage of cells viable, delivered to, and delivery efficiency using different electrolytes. The electrolytes are listed underneath the graphs with the culture chamber electrolyte on top and the cargo chamber electrolyte on bottom. **J.** Percentage of cells viable, delivered to, and delivery efficiency using different seeding densities. Error bars are present in 5H-5J and represent the standard error of the mean ($n \geq 3$). Statistical significance was calculated using a one-way analysis of variance (ANOVA) followed by Tukey's multiple comparison post-hoc test. $p < 0.05$ was considered statistically significant. * represents $p < 0.05$, ** represents $p < 0.01$, *** represents $p < 0.001$, and **** represents $p < 0.0001$.

cells were identified by calcein inclusion and total cells were identified by Hoechst 33342 inclusion. Viability, total delivery, and delivery efficiency were quantified using image processing (Figs. S5 and SI). Our viability and delivery percentages are lower than other recent studies, which may be explained by 2 reasons: our system parameters can be further optimized, and when image processing was ambiguous, we sought to underestimate delivery. For each experiment, representative images and quantitative graphs are shown (representative images for the voltage experiment are shown in Figs. S6 and SI). All experiments used waveforms with 400 pulses, 3 ms pulse duration, and 500 ms pulse interval. These waveform parameters were based on waveform parameters from a study by Mukherjee et al. which utilized a similar PSEP device (Mukherjee et al., 2020). Cells were electroporated in the incubator (Figs. S7 and SI) to maintain viability. The standard conditions for these experiments were voltage set at 8V, a seeding density of 150,000 cells·cm^{-2}, and DMEM used in the cell culture chamber while HOB was used in the cargo chamber. The influence of voltage, electrolytes, and seeding density on delivery and viability were investigated one at a time with all other variables kept at the standard conditions.

Our model could not be used directly to predict the necessary voltage for electroporation because our model uses room temperature PBS rather than DMEM and HOB at 37°C. The EEI and bulk electrolyte impedances were measured approximately 2 times higher for the electroporation conditions, decreasing the TMP by about half. Using a 0.5 correction factor to account for this 50% decrease and the TMP comprising 80% of the cell monolayer mean the true TMP is approximately 40% of the cell monolayer voltage predicted by our model. 0.2–1V has been stated as the TMP necessary for electroporation to occur (Wang et al., 2010). For a 6V, 3 ms duration waveform applied to room temperature PBS, our model predicts a peak cell monolayer voltage of 1.7V and an average of 1.3V. For a 4V, 3 ms duration waveform applied to room temperature PBS, our model predicts a peak cell monolayer voltage of 1.1V and an average of 0.7V. After applying the 0.5 correction factor mentioned earlier to account for DMEM at 37°C, our model predicted that 4V would produce an average TMP of 0.3V and 6V would produce an average TMP of 0.6V, values in the range of critical TMP estimated by previous studies (Figs. S8 and SI). Corresponding estimations of the electric field delivered to the cells at 4, 6 and 8V are shown in Table S4.

To assess our model's ability to predict the necessary voltage for electroporation to occur, voltages ranging from 0V to 15V were applied. At 0V, no delivery and approximately 100% viability were observed, while at 8V significant delivery and cell death were observed (Fig. 4H). 6V was the minimum voltage where delivery occurred. We observed that 6V allowed delivery of BSA through electroporation, whereas 4V was insufficient for delivery. Our model predicted an applied voltage of 4–6 V would be necessary for electroporation, which was confirmed by our experimental results. This is one example of how our model can be used to expedite and optimize experimental parameter selection, however future studies may benefit from numerous predictive aspects of a circuit model. Understanding the various system impedances and how they affect the voltage distribution through the system allows aspects such as electrode materials and geometry, substrate geometry, and waveform selection to be tailored to cargo transport and pore formation. Moreover, by understanding what voltage is present at different points in the system and comparing it to electroporation outcomes, models of cargo transport and pore formation can be improved.

In addition to the influence of voltage on electroporation outcomes, we evaluated the influence of different electrolytes in the cell culture chamber and cargo chamber. When comparing electrolytes, DMEM in the cell culture chamber and HOB in the cargo chamber resulted in the highest delivery efficiency (Fig. 4A–C, 4I). Electrokinetic transport may explain our observations when using different electrolytes for electroporation. Previously, Mukherjee and colleagues (Mukherjee et al., 2018) found HOB increased PSEP delivery and proposed that the increase was primarily due to an increase in cell membrane tension from osmotic swelling. Accordingly, HOB in the cell culture chamber should result in greater delivery due to a larger surface area of the cell membrane exposed to the HOB and thus higher osmotic swelling. Interestingly, HOB in the cell culture chamber required a higher voltage of 15V to induce the same delivery as when HOB was used in the cargo chamber. The change in voltage cannot be explained by conductivity because PBS and DMEM have similar conductivity (Figs. S9 and SI). Lower viability was also observed, likely due to DMEM providing a more natural environment than HOB. As a result, we propose that the increase in delivery from using HOB for PSEP is primarily due to an increase in the zeta potential and a corresponding increase in electrophoresis of the cargo, not from osmotic swelling. The zeta potential of BSA is more negative in low molarity KCl electrolytes than higher molarity NaCl electrolytes which are similar to HOB and PBS, respectively (Salgin et al., 2012). An increase in zeta potential magnitude increases electrophoretic mobility and decreases particle clustering, providing easier transport through the channels and into the cell membrane pores.

Delivery increased and viability decreased with increasing seeding density (Fig. 4D–G, 4J). Very little delivery occurred until a seeding density of 150,000 cells/cm^2, the same seeding density where the maximum cell monolayer impedance was observed. PSEP dependency on high confluency was previously predicted (Mukherjee et al., 2018), but not supported experimentally. Our measurements provide experimental support for this prediction. There is a low impedance dependency on confluency until almost 100% confluency due to low cell monolayer impedance. This may be because the cell monolayer impedance is in parallel with exposed channels, which have a much lower impedance. As the exposed area decreases, the exposed area impedance increases and a larger percentage of the electrical current travels through the cell monolayer. At 200,000 cells/cm^2, the decrease in viability may be due to increased stress from culture at such a high seeding density. A study using the similar method of nanostraw electroporation concluded that confluency had no significant impact on electroporation (Cao et al., 2018). Until impedance measurement driven circuit modeling of nanostraw electroporation has been performed, it is unknown whether the discrepancy is due to differences in system impedance, differences in the applied waveform, or fundamental differences between PSEP and nanostraw electroporation.

4. Conclusion

Although porous substrate electroporation, or PSEP, has been demonstrated in numerous biological applications, the underlying physical processes influencing successful delivery are not well understood. We have developed for the first time a circuit model of the PSEP system using experimental data which helps to explain the intermediate processes that occur between the application of voltage and the delivery of cargo into the cell. One intermediate process is the formation of a critical transmembrane potential capable of permeabilizing the cell membrane, which we were able to predict and demonstrated that it aligned with our experimental data and the experimental data of others. Another intermediate process is the electrokinetic transport of cargo through the channels in the substrate, which we showed plays a significant role in the delivery of cargo into the cell. A greater understanding of these processes will facilitate improvements in the design of PSEP systems and improved delivery to difficult cells such as stem and primary cells. While our circuit model provides greater insight to the PSEP process, it can be improved to increase the accuracy of its predictions. Going forward, better models coupled with impedance measurements of samples prior to electroporation will improve tailoring of waveforms to different systems and applications.

CRediT authorship contribution statement

Justin R. Brooks: Conceptualization, Methodology, Investigation, Writing – original draft, Writing – review & editing. **Ikhlaas Mungloo:**

Methodology, Investigation. **Siamak Mirfendereski:** Methodology, Investigation, Writing – original draft, Writing – review & editing. **Jacob P. Quint:** Methodology, Investigation. **Dominic Paul:** Methodology, Investigation. **Arian Jaberi:** Methodology, Investigation. **Jae Sung Park:** Writing – original draft, Writing – review & editing. **Ruiguo Yang:** Conceptualization, Writing – original draft, Writing – review & editing, Supervision.

Declaration of competing interest

The authors declare that they have no known competing financial interests or personal relationships that could have appeared to influence the work reported in this paper.

Acknowledgments

We acknowledge the funding support from the NSF (Awards 1826135, 1936065), the NIH National Institutes of General Medical Sciences P20GM113126 (Nebraska Center for Integrated Biomolecular Communication) and P30GM127200 (Nebraska Center for Nanomedicine), and the Nebraska Collaborative Initiative. Manufacturing and characterization analysis were performed at the NanoEngineering Research Core Facility (NERCF), which is partially funded by the Nebraska Research Initiative. Zeta potential analysis was performed at Pannier Lab, University of Nebraska-Lincoln.

Appendix A. Supplementary data

Supplementary data to this article can be found online at https://doi.org/10.1016/j.bios.2021.113862.

References

Aycock, K.N., Davalos, R.V., 2019. Bioelectricity 1 (4), 214–234.
Bertani, P., Chang, L.Q., Gallego-Perez, D., Malkoc, V., Lee, L.J., Lu, W., 2015. pp. 83-84.
Bertrand, C., Durand, D., Saidel, G., Laboisse, C., Hopfer, U., 1998. Biophys. J. 75 (6), 2743–2756.
Brooks, J., Minnick, G., Mukherjee, P., Jaberi, A., Chang, L., Espinosa, H.D., Yang, R., 2020. Small, p. 2004917 n/a(n/a).
Cacopardo, L., Costa, J., Giusti, S., Buoncompagni, L., Meucci, S., Corti, A., Mattei, G., Ahluwalia, A., 2019. Biosens. Bioelectron. 140, 111340.
Cao, Y., Chen, H., Qiu, R., Hanna, M., Ma, E., Hjort, M., Zhang, A., Lewis, R.S., Wu, J.C., Melosh, N.A., 2018. Sci. Adv. 4.
Cao, Y., Ma, E., Cestellos-Blanco, S., Qiu, R., Su, Y., Doudna, J.A., Yang, P., 2019a. Proceedings of the National Academy of Sciences of the United States of Am 116, 22911.
Cao, Y., Ma, E., Cestellos-Blanco, S., Zhang, B., Qiu, R., Su, Y., Doudna, J.A., Yang, P., 2019b. Proc. Natl. Acad. Sci. Unit. States Am. 116 (16), 7899.
Cereijido, M., Robbins, E., Dolan, W., Rotunno, C., Sabatini, D., 1978. J. Cell Biol. 77 (3), 853–880.
Cervia, L.D., Yuan, F., 2018. Mol. Pharm. 15 (9), 3617–3624.
Chang, L., Bertani, P., Gallego-Perez, D., Yang, Z., Chen, F., Chiang, C., Malkoc, V., Kuang, T., Gao, K., Lee, L.J., Lu, W., 2016a. Nanoscale 8 (1), 243–252.
Chang, L., Gallego-Perez, D., Chiang, C.-L., Bertani, P., Kuang, T., Sheng, Y., Chen, F., Chen, Z., Shi, J., Yang, H., Huang, X., Malkoc, V., Lu, W., Lee, L.J., 2016b. Small 12 (43), 5971–5980.
Chang, L., Gallego-Perez, D., Zhao, X., Bertani, P., Yang, Z., Chiang, C.-L., Malkoc, V., Shi, J., Sen, C.K., Odonnell, L., Yu, J., Lu, W., Lee, L.J., 2015a. Lab Chip 15 (15), 3147–3153.
Chang, L., Howdyshell, M., Liao, W.-C., Chiang, C.-L., Gallego-Perez, D., Yang, Z., Lu, W., Byrd, J.C., Muthusamy, N., Lee, L.J., Sooryakumar, R., 2015b. Small 11 (15), 1818–1828.
Chang, L., Li, L., Shi, J., Sheng, Y., Lu, W., Gallego-Perez, D., Lee, L.J., 2016c. Lab Chip 16, 4047–4062.
Chen, Z., Akenhead, M.A., Sun, X., Sapper, H., Shin, H.Y., Hinds, B.J., 2016. Advanced Healthcare Materials 5 (16), 2105–2112.
Cornelius, T.W., Apel, P.Y., Schiedt, B., Trautmann, C., Toimil-Molares, M.E., Karim, S., Neumann, R., 2007. Nucl. Instrum. Methods Phys. Res. Sect. B Beam Interact. Mater. Atoms 265 (2), 553–557.
Dong, Z., Jiao, Y., Xie, B., Hao, Y., Wang, P., Liu, Y., Shi, J., Chitrakar, C., Black, S., Wang, Y.-C., Lee, L.J., Li, M., Fan, Y., Chang, L., 2020. Microsyst. NanoEng. 6 (1), 2.
Epelboin, I., Keddam, M., Lestrade, J., 1973. Faraday Discuss. Chem. Soc. 56, 264–275.
Erben, M., Decker, S., Franke, H., Galla, H.-J., 1995. J. Biochem. Biophys. Methods 30 (4), 227–238.
Fasmin, F., Srinivasan, R., 2017. J. Electrochem. Soc. 164 (7), H443–H455.
Fei, Z., Hu, X., Choi, H.-w., Wang, S., Farson, D., Lee, L.J., 2010. Anal. Chem. 82 (1), 353–358.
Fei, Z., Wang, S., Xie, Y., Henslee, B.E., Koh, C.G., Lee, L.J., 2007. Anal. Chem. 79 (15), 5719–5722.
Fei, Z., Wu, Y., Sharma, S., Gallego-Perez, D., Higuita-Castro, N., Hansford, D., Lannutti, J.J., Lee, L.J., 2013. Anal. Chem. 85 (3), 1401–1407.
Gianulis, E.C., Lee, J., Jiang, C., Xiao, S., Ibey, B.L., Pakhomov, A.G., 2015. Sci. Rep. 5 (1), 13818.
Huang, Y., Rubinsky, B., 2001. Sens. Actuators, A 89, 242–249.
Kang, J., Wen, J., Jayaram, S.H., Yu, A., Wang, X., 2014. Electrochim. Acta 115, 587–598.
Kang, W., Yavari, F., Minary-Jolandan, M., Giraldo-Vela, J.P., Safi, A., McNaughton, R.L., Parpoil, V., Espinosa, H.D., 2013. Nano Lett. 13 (6), 2448–2457.
Kemery, P.J., Steehler, J.K., Bohn, P.W., 1998. Langmuir 14 (10), 2884–2889.
Khine, M., Ionescu-Zanetti, C., Blatz, A., Wang, L.-P., Lee, L.P., 2007. Lab Chip 7 (4), 457–462.
Lasia, A., 2014. Springer Science+Business Media, New York.
Linz, G., Djeljadini, S., Steinbeck, L., Köse, G., Kiessling, F., Wessling, M., 2020. Biosens. Bioelectron. 165, 112345.
Mayer, S., Geddes, L.A., Bourland, J.D., Ogborn, L., 1992. Med. Biol. Eng. Comput. 30 (5), 538–542.
Mukherjee, P., Berns, E.J., Patino, C.A., Hakim Moully, E., Chang, L., Nathamgari, S.S.P., Kessler, J.A., Mrksich, M., Espinosa, H.D., 2020. Small 16 (26), e2000584.
Mukherjee, P., Nathamgari, S.S.P., Kessler, J.A., Espinosa, H.D., 2018. ACS Nano 12 (12), 12118–12128.
Ruzgys, P., Novickij, V., Novickij, J., Šatkauskas, S., 2019. Bioelectrochemistry 127, 87–93.
Salgin, S., Salgin, U., Bahadir, S., 2012. Int. J. Electrochem. Sci 7 (12), 12404–12414.
Shi, J., Ma, Y., Zhu, J., Chen, Y., Sun, Y., Yao, Y., Yang, Z., Xie, J., 2018a. Molecules 23 (11), 3044.
Shi, J., Ma, Y., Zhu, J., Chen, Y., Sun, Y., Yao, Y., Yang, Z., Xie, J., 2018b. Molecules 23 (11).
Shiva Nathamgari, S.P., Mukherjee, P., Kessler, J.A., Espinosa, H.D., 2019. Proceedings of the National Academy of Sciences of the United States of Am 116, 22909–22910.
Stewart, M.P., Sharei, A., Ding, X., Sahay, G., Langer, R., Jensen, K.F., 2016. Nature 538 (7624), 183–192.
Susloparova, A., Koppenhöfer, D., Vu, X.T., Weil, M., Ingebrandt, S., 2013. Biosens. Bioelectron. 40 (1), 50–56.
Wang, M., Orwar, O., Olofsson, J., Weber, S.G., 2010. Anal. Bioanal. Chem. 397 (8), 3235–3248.
Wegener, J., Sieber, M., Galla, H.-J., 1996. J. Biochem. Biophys. Methods 32 (3), 151–170.
Yang, C., 2018. University of California, Irvine.
Zhang, L., Hu, X., Wang, Z., Sun, F., Dorrell, D.G., 2018. Renew. Sustain. Energy Rev. 81, 1868–1878.
Zhang, X., Lu, J., Yuan, S., Yang, J., Zhou, X., 2017. J. Power Sources 345, 21–29.